



Synergistic electrocatalysis of crystal facet and O-vacancy for enhancing urea synthesis from nitrate and CO₂

Zhengyi Li ^{a,1}, Peng Zhou ^{b,1}, Min Zhou ^a, Hao Jiang ^a, Hu Li ^{a,*}, Shengqi Liu ^a, Heng Zhang ^a, Song Yang ^{a,*}, Zehui Zhang ^{b,*}

^a National Key Laboratory of Green Pesticide, Key Laboratory of Green Pesticide and Agricultural Bioengineering, Ministry of Education, State-Local Joint Laboratory for Comprehensive Utilization of Biomass, Center for R&D of Fine Chemicals, Guizhou University, Guiyang 550025 Guizhou, China

^b Key Laboratory of Catalysis and Energy Materials Chemistry of Ministry of Education, South-Central University for Nationalities, Wuhan 430074, China



ARTICLE INFO

Keywords:
Urea electrosynthesis
C–N coupling
Synergistic catalysis
CO₂ utilization
Nitrogen fixation

ABSTRACT

One-pot green urea electrosynthesis from CO₂ and nitrogenous pollutants via the co-reductive C–N coupling route under ambient conditions is prospective to replace the traditional urea synthesis process. Here, a bifunctional indium hydroxide (Vo-S-IO-6) bearing oxygen vacancy (Vo) sites on {100} facets was developed to markedly enable urea synthesis (unprecedented faradaic efficiency of 60.6% with a high production rate of 910.4 µg h⁻¹ mg⁻¹cat.) from NO₃⁻ and CO₂ by subtly integrating facet and defect engineering. In-O-x-O-In (x = C or N) configuration and Vo in Vo-S-IO-6 provided dual active sites for the adsorption and activation of NO₃⁻ and CO₂ to exclusively form *NO₂ and *CO₂ species, respectively, which ensured highly selective C–N coupling. Moreover, theoretical calculations elaborated that Vo-induced local electron reconstruction accelerated the protonation rate-determining step, thus lowering overall energy barriers. This work offers a design strategy of synergistic electrocatalysts based on geometrical nature for efficient urea synthesis.

1. Introduction

Elevating atmospheric CO₂ concentrations caused by the fossil industry has led to a series of severe environmental and social problems, such as climate change, sea level rise, and crop failures [1]. Reducing CO₂ emission is now a major challenge faced by human society, and one of the key points to overcoming the issues associated with CO₂ is to find effective methods for the upgrading of CO₂ into value-added chemicals for our society [2,3]. Due to the highly inert properties of CO₂ molecules, chemical reactions with CO₂ to produce chemicals or fuels are generally performed under harsh operating conditions (e.g., elevated temperature, and elevated pressure). The electrochemical route to produce chemicals is promising for replacing the traditional energy-intensive and high-emission methods for utilization of fossil fuels, considering its sustainable energy sources, more controllable reaction selectivity, and mild conditions [4,5]. The cleavage and formation of chemical bonds, especially C–O and H–O bonds, in H₂O electrolysis and electrocatalytic CO₂ reduction have been extensively investigated [1]. As one of the emerging approaches for efficient CO₂

valorization, electrification of many important thermochemical processes including C–N bond formation [6], C–H activation [7], and oxidation [8,9] in the chemical industry shows great potential to get economically feasible products, such as urea, amines, and amides [10–12].

Urea, an alluring product to allow N-integrated CO₂ fixation, is one of the most vital nitrogen fertilizers in the agricultural industry and a crucial feedstock for the manufacture of drugs, plastics, and chemical products with around US \$75 billion in market size [12–14]. Up to now, urea is still generated with a series of energy-intensive processes involving methane steam reforming [15], Haber–Bosch process [16], and Bosch–Meiser process [12]. Thereinto, the Haber–Bosch process is associated with around 2% of worldwide energy consumption and generates about 1% of global CO₂ emissions [16,17]. In order to achieve satisfactory reaction rates, elevated temperatures (400–500 °C) and pressure (100–300 bar) are needed to push the reaction equilibrium toward the formation of urea [12]. The direct coupling of inert N₂ and CO₂ under ambient conditions via electrocatalysis provides a sustainable and economical way for urea production [18]. In electrocatalytic

* Corresponding authors.

E-mail addresses: hli13@gzu.edu.cn (H. Li), jhzx.msm@gmail.com (S. Yang), zehuizh@mail.ustc.edu.cn (Z. Zhang).

¹ These authors contributed equally to this work.

reactions, the conversion process (e.g., pathways and rates) can be conveniently controlled through well-tailored catalytic sites and the applied voltage window. To overcome the difficulties of inert N₂ in dissociation (941 kJ mol⁻¹) in urea electrosynthesis, the local electrophilic-nucleophilic intervals are constructed by adjusting the interface/surface structure and optimizing the electronic structure to enhance the adsorption and activation of inert substrates [19–22]. Further, the host-guest intermolecular interaction has been used to reduce the electron filling of σ orbital in *N₂ and *CO intermediates to promote C–N coupling [23]. Nevertheless, the extremely low solubility of N₂ is still distressing. Nitrogenous pollutants, especially nitrate (NO₃), have been regarded as good alternatives to N₂ in the electrosynthesis of urea, because of its comparatively low N = O bond dissociation energy (204 kJ mol⁻¹) and high solubility. The key challenges in this reaction are the complex 16-electron transfer and 18-proton coupling processes in NO₃⁻-integrated electrocatalytic CO₂ reduction [24–26], and thus the undesired protonation of key intermediates rather than C–N coupling occurs easily, resulting in the production of large amounts of byproducts such as NH₃, HCOOH, and CO. Therefore, the development of a novel electrocatalytic system to effectively promote the coupling of the intermediates from the NO₃⁻ (NO₃RR) reduction reaction and CO₂ reduction reaction (CO₂RR) is necessary to yield urea with high selectivity. For instance, the *CO and *NH₂ intermediate from the co-reduction reaction of NO₃⁻ and CO₂ can efficiently yield urea [26]. Furthermore, the direct coupling of *CO₂ and *NO₂ at the early stage can further boost the selectivity of urea electrosynthesis [24]. Since both CO₂RR and NO₃RR involve the adsorption and desorption of oxygen species, the catalytic process for urea electrosynthesis can be controlled by the adsorption energies of carbon species (E_{a,*C}; e.g., *CO and *CO₂) and nitrogen species (E_{a,*N}; e.g., *NH₂ and *NO₂). Currently, most of the studies have focused on the activation of substrate molecules and sub-reactions to obtain the above-mentioned coupling species, while the recognition and understanding of C–N coupling sites have been little studied [24–26].

It is well known that the efficiency of an electrocatalyst can be adjusted by the active site and local electronic structure [27,28]. For example, Lv et al. reported a crystal facet engineering strategy to enhance the selectivity of urea [24]. By tuning the exposure of In(OH)₃ dominant active facets, which influence E_{a,*C} and E_{a,*N} significantly, selective coupling of the intermediates becomes possible [29,30]. Noticeably, ideal active facets should have a defined density of state (DOS) that appropriately duplicates the orbitals of the reactive species [31]. Although the selectivity of urea electrosynthesis can be efficiently boosted by designing a reliable C–N coupling platform on a specific facet, a high energy barrier still needs to be overcome, leading to a sluggish reaction rate [24]. In this regard, adjusting the local electronic environment can be an applicable method to improve the intrinsic activity of electrocatalysts [18,32–34]. As far as we know, the development of a highly efficient catalyst for urea electrosynthesis combining the great advantages of both Vo and facet is rarely reported, with little understanding of the synergistic effect of facet and Vo in urea electrosynthesis.

In this work, facet and defect engineering was integrated to develop a highly efficient Vo-rich indium hydroxide nanocube catalyst with dominant {100} facets (denoted as Vo-S-IO) for electrosynthesis of urea from the reductive coupling of NO₃⁻ and CO₂. The highest faradaic efficiency (FE) reached 60.6% with a production rate of 910.4 $\mu\text{g h}^{-1} \text{mg}_{\text{cat}}^{-1}$ at -0.6 V in CO₂-saturated 0.1 M KNO₃ aqueous solution. The reaction scope was extended for the synthesis of other organic amines. Density functional theory (DFT) calculations confirmed that the dominant {100} facets and rich Vo were responsible for the superior catalytic efficiency. *In situ* attenuated total reflection Fourier transform infrared spectroscopy (ATR-FTIR) indicated that urea was yielded via the coupling of *CO₂ and *NO₂ and further protonation.

2. Experimental

2.1. Preparation of S-IO, Vo-S-IO, and M-IO

A simple solvothermal method was applied for fabricating IO nanocubes with {100} facets (denoted as S-IO). In a typical preparation procedure, 10 mL NaOH solution (1 M) was added to 20 mL ethylene glycol containing 0.586 g (2.0 mmol) InCl₃·4 H₂O. The precursor metal solution was treated by solvothermal method at 200 °C for 24 h. The white solid was obtained by centrifugation and washed with ethanol (3 × 20 mL). The Vo-S-IO catalysts were prepared by adjusting the glycol/NaOH solution (v/v) to 4, 6, 8, and 10, which are named Vo-S-IO-4, Vo-S-IO-6, Vo-S-IO-8, and Vo-S-IO-10, respectively. M-IO was obtained using a similar method as S-IO but varying the solvent system and base concentration, in which 10 mL NaOH aqueous solution (0.5 M) was added to 20 mL mixed solvent (ethanol: glycol (v/v) = 9:1) containing 0.586 g (2.0 mmol) InCl₃·4 H₂O. Chemicals and materials are shown in [Supporting Information](#).

2.2. Preparation of S-IO, Vo-S-IO, and M-IO modified electrodes

8 mg of S-IO, Vo-S-IO, or M-IO and 2 mg carbon black were dispersed in 800 μL of the mixed solution of ethanol and Nafion (5 wt% aqueous solutions, 760:40 v/v) to constitute a homogeneous ink solution by sonication for 1 h. Subsequently, 10 μL of catalyst ink was dropped on a carbon paper (TGP-H-090, 1 × 1 cm^2) and used as working electrodes with the loading of approximately 0.1 mg cm^{-2} after natural drying.

2.3. Electrochemical tests

All electrochemical experiments were undertaken at 25 °C using a CHI 630E electrochemical workstation. Voltammetric experiments and bulk electrolysis experiments were conducted in an H-cell separated by a pretreated Nafion 117 membrane with catalysts modified carbon paper as the working, a Pt sheet (1 × 1 cm^2), and Ag/AgCl (3.5 M KCl) as the counter and reference electrodes, respectively. Voltammetric experiments were conducted with a scan rate of 10 mV s⁻¹ and the imposed potentials were converted to RHE scale using the Nernst equation of form E (versus RHE) = E (versus Ag/AgCl) + 0.197 V + 0.059 V × pH. For urea electrosynthesis, both chamber of the H-cell was filled with 30 mL CO₂-saturated 0.1 M KNO₃. During electrolysis, the electrolyte in the cathode chamber was stirred at a speed of 300 rpm and the purified CO₂ was consecutively supplied into the cathode chamber at a continuous rate of 30 mL min⁻¹. Electrochemical NO₃⁻RR tests were performed in 0.1 M KNO₃ without CO₂ as feeding gas. For the electrosynthesis of formamide, the CO₂-saturated 0.1 M KHCO₃ solution was used as the electrolyte in the anodic compartment, and the CO₂-saturated 0.1 M KHCO₃ containing 20 mM nitrogenous reagent (nitro compound) was used as the electrolyte in the cathodic compartment. Other characterizations, measurements, and computational methods are supplied in [Supporting Information](#).

2.4. Quantification of various reduction products

2.4.1. Quantification of urea (CO(NH₂)₂)

Urea was quantified using the diacetyl monoxime method. Acid-ferric solution (solution A) was prepared from a mixture of phosphoric acid (concentrated, 100 mL), sulfuric acid (concentrated, 300 mL), ferric chloride (100 mg), and deionized water (600 mL). The diacetylmonoxime (DAMO)-thiosemicarbazide (TSC) aqueous solution (solution B) consists of 0.005 wt% DAMO and 0.1 wt% TSC. Then 1 mL of the reaction electrolyte was added to the chromogenic agent containing 2 mL solution A and 1 mL solution B, and the mixture was statically maintained for 25 min at 100 °C. The absorbance was measured at the wavelength of 525 nm using UV-vis spectroscopy ([Fig. S9a](#)). The absorbance curve for calculated concentration was calibrated with

standard urea solution (Fig. S9b).

2.4.2. Quantification of ammonia (NH_3)

Ammonia was quantified using the indophenol blue method. 2 mL NaOH (1.0 M) aqueous solution containing salicylic acid (5 wt%) and potassium sodium tartrate tetrahydrate (5 wt%) was added to a mixed solution of NaClO (0.05 M, 0.5 mL) and sodium nitroferricyanide (1 wt %, 0.05 mL) to form a chromogenic agent. After the electrolysis, the reaction electrolyte (2 mL) was taken from the cathode chamber and mixed with the chromogenic agent, and the mixture was placed for 1 h in the dark. The absorbance at 670 nm was recorded by UV-vis. The absorbance curve for calculated concentration was calibrated with a standard NH_4Cl solution (Fig. S13).

The 0.1 M K^{15}NO_3 (99 atom%) was used as the feeding N-source without CO_2 for the isotopic labeling nitrate reduction experiments to clarify the source of ammonia. After electroreduction, 0.5 mL of

electrolyte with obtained $^{15}\text{NH}_4^+$ was taken out, followed by the addition of 50 μL deuterium oxide (D_2O), which underwent further quantification by ^1H NMR (500 MHz) with external standards of maleic acid (0.02 g). ^1H NMR verified that the indophenol blue method was reliable for qualitative and quantitative analysis of NH_3 (Fig. S15).

2.4.3. Quantification of nitrite ions (NO_2^-)

NO_2^- was quantified by the Griess reaction. The Griess reagent was prepared by dissolving NED (0.1 g), sulfonamide (1.0 g), and H_3PO_4 (2.94 mL) in deionized H_2O (50 mL). After the reaction, 1 mL of the reaction electrolyte was collected from the cathode chamber and added to 3 mL water-diluted chromogenic agent (1:2, v/v), and the mixture was allowed to react for 10 min at room temperature. The absorbance at 540 nm was recorded UV-vis. The absorbance curve for calculated concentration was calibrated with standard KNO_2 solutions (Fig. S16).

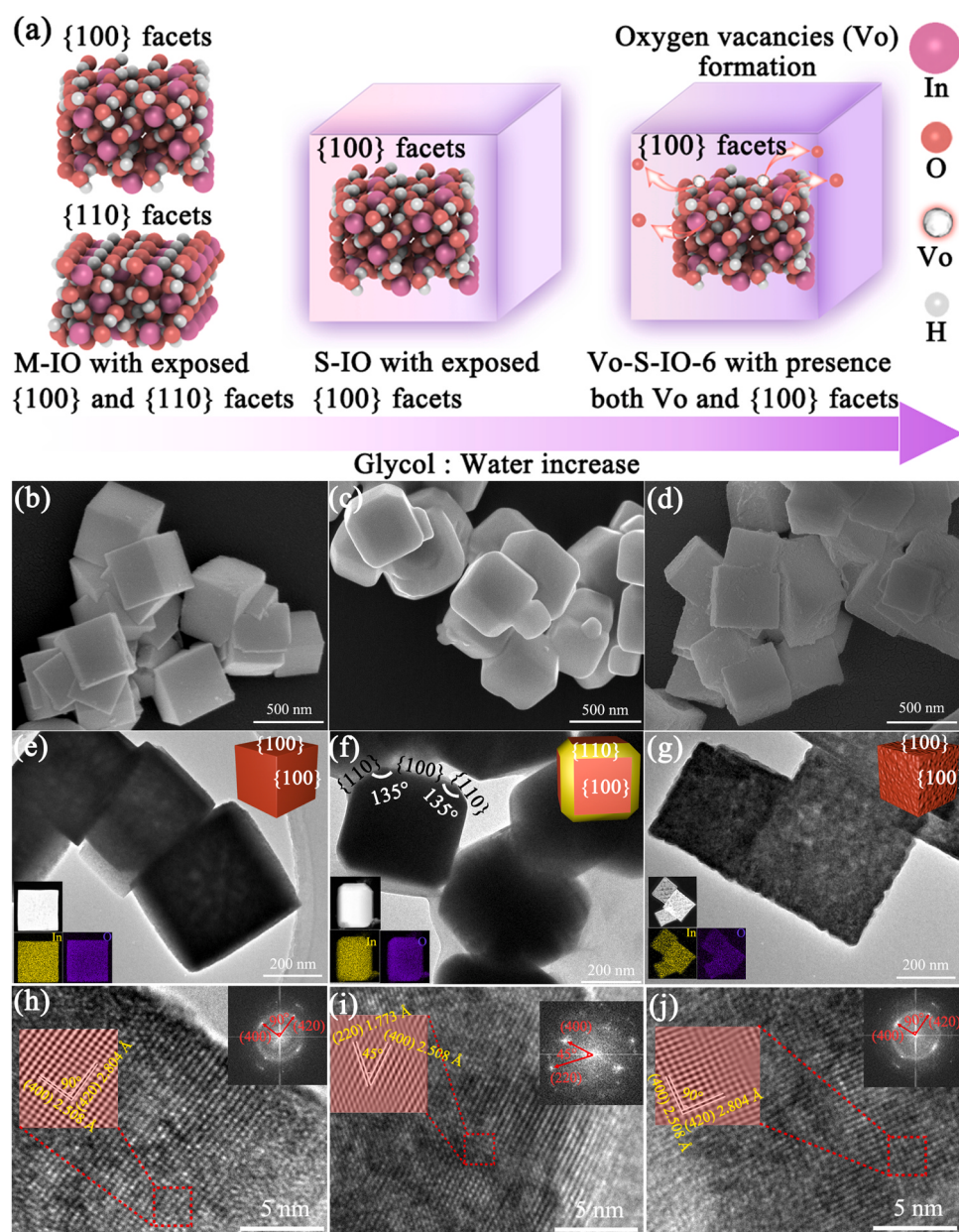


Fig. 1. (a) Schematic diagram for preparation of M-IO, S-IO, and Vo-S-IO-6. (b-d) SEM images, (e-g) TEM images with corresponding TEM-mappings embedded, and (h-j) HRTEM images of M-IO, S-IO, and Vo-S-IO-6. The insets on the upper right in (h-j) are the fast-Fourier transform (FFT) patterns of S-IO, M-IO, and Vo-S-IO-6, and the red regions are the IFFT images from the circled boxes.

2.4.4. Quantification of formic acid (HCOOH)

Quantitative analysis of HCOOH content was conducted by ion chromatograph (Dionex ICS-600) equipped with an AS11-HC chromatographic column (250×4 mm). Testing conditions were optimized, and the eluent was 3 mM NaOH solution at a flow rate of 1.5 mL min^{-1} .

2.4.5. Other gas products (carbon monoxide (CO), hydrogen (H₂), and dinitrogen (N₂)) quantification

The amounts of CO, H₂, and N₂ were quantified by an online gas chromatograph (GC, Agilent 7890B) equipped with TCD and FID. The gas chromatography was instrumented with a molecular sieve 5 A and a porapak Q column. Argon was employed as the carrier gas.

3. Results and discussion

3.1. Characterization of as-prepared catalysts

The Vo-S-IO catalyst was simply prepared via a facile solvent-thermal-reduction method, as described in Fig. 1a. The exposed facets of indium hydroxide (IO) showed strong dependence on the glycol content of the solvent used for synthesis. For comparison, indium hydroxide nanocube with mixed {100} and {110} facets (M-IO) or with dominant {100} facets (S-IO; with the glycol to water volume ratio of 2:1) was also prepared. The morphology of the electrocatalysts varies greatly due to the coating of different facets. Scanning electron microscopy (SEM) and transmission electron microscopy (TEM) images of S-IO nanocrystals show a well-defined nanocube morphology with a particle size of 300–400 nm (Fig. 1b&e). The corresponding TEM mappings illustrate the homogeneous allocation of In and O elements on the entire nanocube (Fig. 1e-f, inset), demonstrating that the active sites over the catalysts are evenly dispersed. The selected-area electron diffraction (SAED) patterns and high-resolution TEM (HRTEM) were employed to explore exposed lattice planes of the as-prepared electrocatalysts. The clear diffraction rings corresponding to (200), (220), (222), (400), (420), and (422) lattice planes were observed (Fig. S2). The inverse fast Fourier transform (IFFT) images (red regions of insert in Fig. 1h-i) show lattice fringes with a lattice spacing of 2.508 and 2.804 Å, which can be classified as (400) and (420) lattice planes of catalysts, respectively (Fig. S3). The surface of an S-IO nanocube shows an interfringe angle of 90°, which is a typical characteristic of {100} facets on the cubic crystal (Fig. 1h) [24]. In addition, the M-IO nanocrystals with a particle size of 300–400 nm possess well-defined and noticeable truncations at the edges, exhibiting a significant difference in contrast with the cube-like S-IO (Fig. 1c). Apart from the {100} facets on an M-IO nanocrystal (Fig. 1f), new facets emerge simultaneously with an angle of 135°. Based on the cubic structure and the edge-truncated morphology of M-IO, the extra facets can be indexed to the {110} facets (Fig. 1f) [24]. For a bcc crystal, its 18-facet polyhedra (Fig. 1e-f) are reported to be enclosed by six {100} facets and twelve {110} facets [35,36]. Meanwhile, the FFT and IFFT image shows interference of 45° crossed between (400) and (220) lattice planes (Figs. S4 and 1i), which are in line with the (100) and (110) facets of the M-IO nanocrystal. Overall, the above discussions unequivocally verify the co-exposure of {100} and {110} facets on M-IO.

To further elucidate the crucial contribution of the electrocatalyst crystal facets and Vo in urea electrosynthesis, S-IO catalysts containing different Vo concentrations were prepared by modulating the relative content of glycol and water, and the obtained electrocatalysts (Vo-S-IO-*n*, *n* is the volume ratio of glycol to water) were denoted as Vo-S-IO-4, Vo-S-IO-6, Vo-S-IO-8, and Vo-S-IO-10. Noteworthily, the well-maintained nanocube structure of Vo-S-IO-*n* can also be found in SEM (Fig. 1d, & Fig. S1) and TEM (Fig. 1g) images. As the ratio of glycol increased, the particle size of the nanocubes became smaller and packed with each other, which was much more distinct by increasing the volume ratio of glycol/water to 8 (Fig. S1). In addition, the SEM image of the representative Vo-S-IO-6 sample became rough upon the introduction of oxygen defects (Fig. 1b vs d). The SAED pattern shows that the

lattice planes of Vo-S-IO-6 (Fig. S2c) are identical to those of S-IO and M-IO (Fig. S2a & b). Also, the interfringe angle of 90° on the surface of Vo-S-IO-6 nanocube with obvious dislocation and distortion was observed (Figs. S5 and 1j) [24], indicating that {100} facets can be well-reserved after introducing Vo. These formed defects may greatly increase the number of active sites and provide a reliable platform to reveal the synergy of crystal facets and Vo in the synthesis of urea from NO₃⁻-integrated electrocatalytic CO₂ reduction.

Meanwhile, electron paramagnetic resonance (EPR) spectroscopy was used to determine the content of Vo in the series of Vo-S-IO-*n* [37]. As shown in Fig. S2, EPR spectra of Vo-S-IO-*n* show the characteristic EPR signal at *g* = 2.003, which is assigned to the electron-deficient oxygen anion species (O₅⁻) [38]. The controlled S-IO sample showed no EPR signal of Vo (Fig. S6), while the intensity of the EPR signal became stronger with the increase of the volume ratio of glycol (Fig. S6). These results suggested that glycol served as the reducing agent in the creation of Vo in indium hydroxide during the thermal treatment process.

X-ray diffraction (XRD) patterns of the as-prepared samples show the characteristic peaks of pristine IO (Joint Committee on Powder Diffraction Standards, JCPDS: 76–1464), without any impure phase (Fig. 2a). The characteristic bragg peaks at 22.2°, 31.6°, 39.0°, 45.4°, 51.1°, and 56.4° are assigned to the (200), (220), (222), (400), (420), and (422) lattice planes of IO, respectively, consisting with the results from HRTEM images and SAED patterns (Fig. 1h-j and Fig. S2). However, the peak intensity of Vo-S-IO-6 significantly became weakened in comparison with that of S-IO, indicating that the introduction of Vo results in low crystallinity [39]. Fourier transform infrared (FT-IR) spectra of the representative samples were then collected. Characteristic adsorption bands for O–H (3235 & 3121 cm⁻¹), –OH (1155 cm⁻¹), and In–O (782 & 499 cm⁻¹) bonds were all found in FT-IR spectra of IO, S-IO, and Vo-S-IO-6 (Fig. S7a) [40]. Meanwhile, the absorption sideband of the In–O bond on the catalyst surface was observed at 304 cm⁻¹ by Raman spectroscopy (Fig. S7b) [41]. Importantly, the absorption peak intensity of the In–O bond in Vo-S-IO-6 is significantly reduced compared to that of M-IO and S-IO, which may be caused by the successful introduction of Vo [25].

The surface chemical states of the elements in the prepared samples were analyzed using X-ray photoelectron spectroscopy (XPS) measurements. Binding energies at 452.1 and 444.5 eV in In 3d XPS spectra (Fig. 2b) can be assigned to the spin-orbit split In 3d_{5/2} and In 3d_{3/2}, indicating the dominant presence of In³⁺ on the surface [42]. Compared with M-IO and S-IO, the In 3d orbital of Vo-S-IO-6 shifts towards a lower binding energy (Fig. 2b), implying the increase of the local electron density of In caused by delocalized electrons after oxygen escaping. Meanwhile, the O 1 s XPS spectra of M-IO, S-IO, and S-IO-6 were also fitted into three peaks (Fig. 2c) as follows: lattice oxygen (531.4 eV), surface hydroxyl (532.4 eV), and absorbed water (533.4 eV), respectively [43,44]. In comparison with M-IO and S-IO, the peak area ratio of lattice oxygen in Vo-S-IO-6 was low, and a new characteristic peak at ca. 531.7 eV could be observed in high-resolution O 1 s XPS spectra of Vo-S-IO-6 (Fig. 2c), which is attributed to Vo in the Vo-S-IO-6 catalyst [25]. Moreover, EPR also verified the existence of Vo in the Vo-S-IO-6 (Fig. 2d). In a short brief, all the above characterizations revealed that the inclusion of glycol during the thermal preparation of Vo-S-IO-6 resulted in the successful introduction of oxygen defects.

3.2. Electrosynthesis of urea over different catalysts

The catalytic performance of the as-prepared catalysts towards electrosynthesis of urea was evaluated in an H-type electrolytic cell with a CO₂-saturated 0.1 M potassium nitrate (KNO₃) electrolyte and the potential was controlled by an electrochemical workstation with a three-electrode set-up. Before the electrocatalytic activity test, the linear sweep voltammograms (LSV) were first conducted to estimate the electrochemical response of as-prepared catalysts towards the

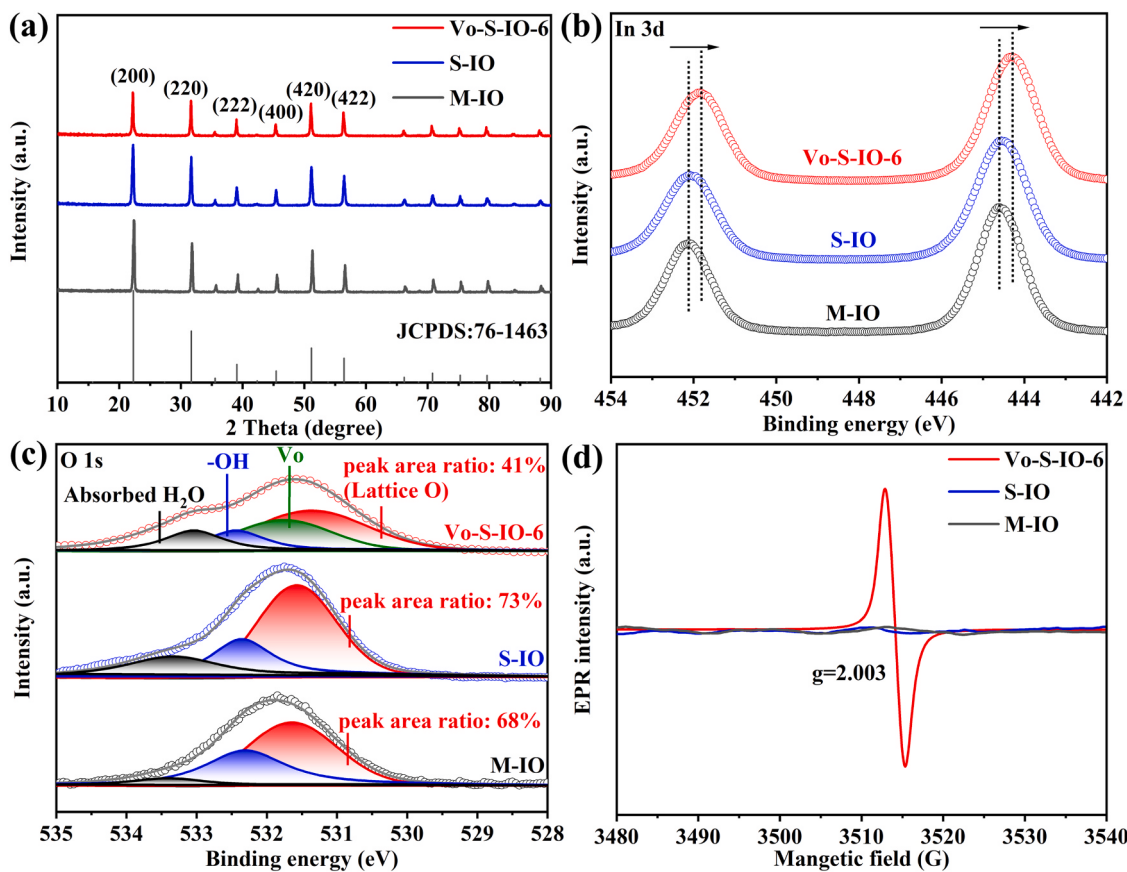


Fig. 2. (a) XRD patterns, (b) In 3d XPS spectra, (c) O 1 s XPS spectra, and (d) EPR spectra of M-IO, S-IO, and Vo-S-IO-6.

electrosynthesis of urea (Fig. 3). For comparison, the LSV curves of the M-IO and S-IO were also collected. Both M-IO and S-IO electrodes displayed a reduction current density contributed by the hydrogen evolution reaction (HER) in the absence of nitrate and CO₂. It is noted that M-IO with mixed {100} and {110} facets exhibited low activity towards the NO₃RR and CO₂RR, and the current density only increased slightly using both NO₃⁻ and CO₂ as feedstock (Fig. 3a). Conversely, the S-IO with dominant {100} facets exhibited high activity towards NO₃RR. Notably, the current density in CO₂-saturated KNO₃ with S-IO catalyst increased significantly and was higher than that with M-IO catalyst (Figs. 3b & 4a). This differentiated response source may be due to the fact that the {100} facets facilitate the adsorption and activation of substrates to construct C–N bonds.

Besides the effect of the facets, the introduction of oxygen defects in the metal oxides or metal hydroxyl oxides was also reported to show positive effect on the electrocatalytic performance of them, mainly including improvement of the bulk phase of materials (e.g., conductivity, and energy band structure) and optimization of surface properties (e.g., surface composition, and molecular adsorption) [27,28]. Therefore, a series of Vo-S-IO-*n* with different contents of oxygen defects were also tested. As shown in Fig. 3c & d, Vo-S-IO-6 derived from S-IO exhibited the highest current density in CO₂-saturated KNO₃ (Fig. 4a). These results suggest that the urea electrosynthesis activity of Vo-S-IO-6 can be significantly improved by {100} facets and Vo.

3.2.1. Effect of facets on the urea electrosynthesis performance

Subsequently, the electrocatalytic activities of M-IO, S-IO, and Vo-S-IO-*n* towards urea synthesis were tested by the chrono-amperometry (CA) in different electrolytes at -0.5 V versus a reversible hydrogen electrode (RHE). Product analysis of the tested reaction mixtures showed that the FEs of the M-IO-catalyzed CO₂RR to CO and NO₃RR were 17.9% and 32.0%, respectively (Fig. S8). Although *CO and *NH₂

are key intermediates in the C–N coupling to produce urea [26], the FE of urea was only 7.7%. In the case of the S-IO catalyst, the FE of CO in CO₂RR was still low (21.7%). But, the total FE of NH₃ and NO₂⁻ in NO₃RR and FE of urea in C–N coupling increased to 58.2% and 22.3%, respectively (Fig. S8). These results suggested that the facets had a pronounced effect on the adsorption and activation of substrates. Notably, the {100} facets are more conducive to urea synthesis, and {100} facet-mediated selective C–N coupling may differ from the conventional co-reduction pathway.

3.2.2. Effect of Vo on the urea electrosynthesis performance

The effect of Vo concentration on the electrosynthesis of urea was further investigated. The FE of urea first increased with the increase of Vo concentration in Vo-S-IO-*n* and then decreased. Among them, the Vo-S-IO-6-catalyzed reaction exhibited the highest FE of urea (33.9%, Fig. S9), indicating that the catalyst activity is not simply correlated positively with its Vo concentration. Moreover, the total FE of NO₃RR to NH₃ and NO₂⁻ with Vo-SI-O-6 and SI-O catalysts was much higher compared to that with M-IO catalysts, indicating that {100} facets are more conducive to NO₃RR. But, the introduction of Vo seemed to inhibit the NO₃RR on {100} facets under the single nitrate reduction conditions (Fig. S8). The improved catalytic efficiency with Vo-SI-O-*n* catalysts might be ascribed to the enhancement of the adsorption of the substrate and key intermediate (*NO₂ or *NH₂) on {100} facets bearing rich Vo sites [24,25]. The Vo-S-IO-10 with excessive oxygen defects resulted in the destruction of the facets, which exhibited low activity toward urea synthesis but was still higher than M-IO (Figs. S8 and S9c&d). These results showed that the presence of Vo individually had a very limited improvement in the performance of urea electrosynthesis. In addition, the adsorption behavior of CO₂ on the M-IO, S-IO and Vo-SI-O-6 surface was investigated by CO₂-TPD (Fig. S10). The peak located at 345 K and 692 K was attributed to physisorbed and chemisorbed CO₂, respectively.

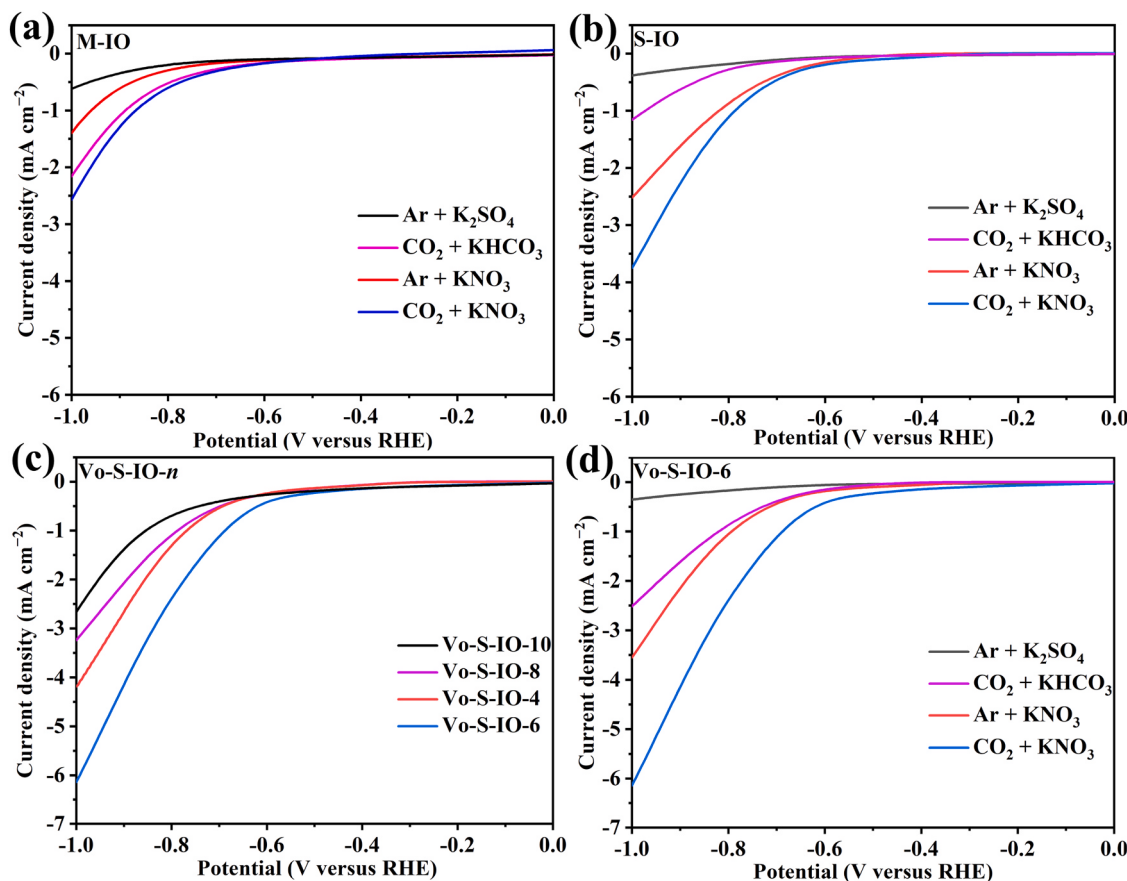


Fig. 3. LSV curves for electrolysis of (a) M-IO, and (b) S-IO in the electrolytes of Ar-saturated 0.1 M K_2SO_4 aqueous solution, CO_2 -saturated 0.1 M KHCO_3 aqueous solution, Ar-saturated 0.1 M KNO_3 aqueous solution, and CO_2 -saturated 0.1 M KNO_3 aqueous solution, respectively, with a scan rate of 10 mV s^{-1} ; (c) Vo-S-IO-*n* in CO_2 -saturated 0.1 M KNO_3 aqueous solution with a scan rate of 10 mV s^{-1} ; and (d) Vo-S-IO-6 under the same conditions as (a) and (b).

Both desorption temperature and peak intensity showed a hierarchical relationship of Vo-SI-O-6 > S-IO > M-IO. Notably, an additional peak was observed at 504 K in Vo-SI-O-6, which may be the result of Vo-adsorbed CO_2 , which is consistent with the finding that Vo can act as a CO_2 adsorption site [45,46], demonstrating that Vo can effectively adsorb CO_2 and thus promote urea electrosynthesis. The enrichment of CO_2 on the catalyst surface benefiting from the co-adsorption of CO_2 on the {100} facets and Vo is prerequisite for the efficient urea electrosynthesis process. Overall, the enhanced activity of Vo-SI-O-6 for urea synthesis results from the synergistic effect of exposed {100} facets and Vo.

The applied potential was then optimized with Vo-S-IO-6 catalyst in CA measurements at an external potential ($-0.5 \sim -0.8 \text{ V}$), and the results are displayed in Fig. S11. The highest production rate of urea reached $910.4 \mu\text{g h}^{-1} \text{ mg}_{\text{cat}}^{-1}$, with FE of 60.6% (Fig. 4b), which can also be verified by ultraviolet-visible (UV-vis) spectra (Fig. S12). The detailed product distribution and the selectivity of N-urea and C-urea ($\text{N}_{\text{urea}}/\text{C}_{\text{urea}}$) at different potentials are summarized in Fig. 4c. Primary by-products, including NH_3 , NO_2^- , H_2 , and CO , derived from the reduction of NO_3^- and CO_2 , were detected at all potentials (Figs. S13–19), while other side products (e.g., N_2 and HCOOH) were not detected. The FE for CO remained low (< 5%) at the applied potential range, which may be due to abundant NO_3^- adsorption sites and a more preferred coupling reaction instead of CO_2 reduction on Vo-S-IO-6. While a more negative applied potential led to a higher FE for NH_3 (9.7% at -0.6 V vs. 20.9% at -0.8 V) and H_2 (11.2% at -0.6 V vs. 37.9% at -0.8 V). This trend can be explained by more available H^* on the catalyst surface at a more negative potential, leading to a higher chance to combine with another H^* or $^*\text{NO}_2$ to produce H_2 or NH_3 . The

$\text{N}_{\text{urea}}/\text{C}_{\text{urea}}$ selectivity was also influenced by the applied potential, reaching their highest value of 75.0% and 94.5%, respectively, at -0.6 V (Fig. 4c).

Two controlled experiments were further carried out to reveal the carbon and nitrogen sources for the electrosynthesis of urea. No urea was detected in the absence of CO_2 or NO_3^- (Fig. 4d), according to the corresponding UV-vis absorbance spectra (Fig. 4d inset), which suggested that CO_2 and NO_3^- were the only carbon and nitrogen sources to access urea, respectively. Electrochemical stability is a vital index for electrocatalysts. The urea yield rate and current density of Vo-S-IO-6 remained nearly unchanged in five consecutive electrocatalytic cycles at -0.6 V (Fig. 4e), which could be attributed to good maintenance of the cubic structure, crystalline phase, and Vo after 5 cycles based on the results of SEM, TEM, XRD, and EPR measurements (Fig. 5). In addition to exhibiting outstanding structural and electrochemical stability (Fig. S20), the activity of Vo-S-IO in electrosynthesis urea was higher than that of other electrocatalysts (Fig. 4f and Table S1). Electrochemically active surface area (ECSA) measurements indicated that the electrochemical double-layer capacitance (C_{dl}) of M-IO and S-IO was very close to that of Vo-S-IO-6 (Fig. 6). In brief, it means that the number of active sites on these three catalysts' surfaces is similar. These results indicated that the predominant activity of Vo-S-IO-6 in electrocatalytic urea production was most likely due to its inherent structural properties tailored through facet and defect engineering.

Inspired by the outstanding performance of VO-S-IO-6 in electrocatalytic co-reduction of both oxidation-state substrates, the concept of reductive C–N coupling was further examined for the electrolysis of organic nitro-compounds with CO_2 . Several nitro compounds were selected as substrates for electrochemical reductive N-formylation

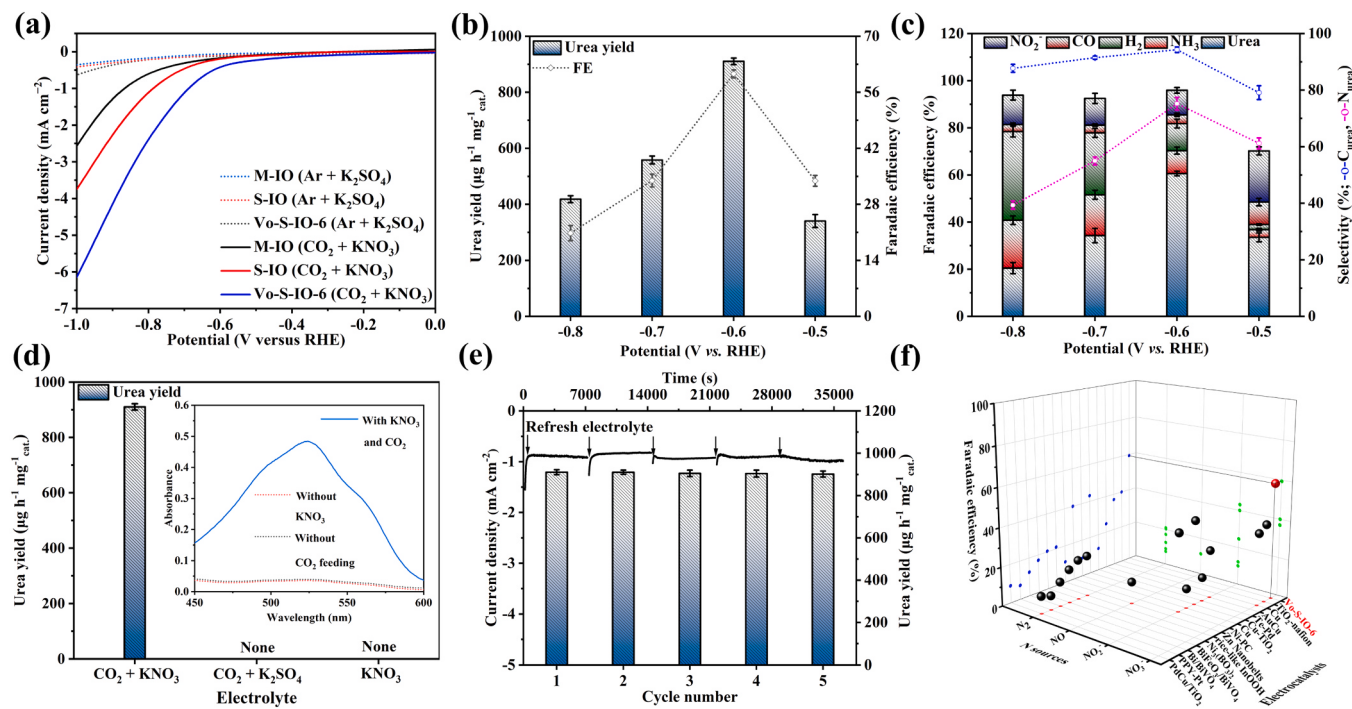


Fig. 4. Electrocatalytic performance of the prepared catalysts in urea electrosynthesis (conditions: electrolyte (0.1 M KNO_3), pH = 3.88, catalyst loading (0.1 mg), and working electrode area ($1 \times 1 \text{ cm}^2$)): (a) LSV curves recorded on the M-IO, S-IO, and Vo-S-IO-6 during urea electrosynthesis and the electroreduction of Vo-S-IO-6 in electrolyte without nitrate or CO_2 . Scan rate = 10 mV s⁻¹. (b) Summary of yields and FEs of urea during urea electrosynthesis with Vo-S-IO-6 catalyst at different potentials after collecting -7.65 C of charge. (c) Summary of results of urea electrosynthesis catalyzed by Vo-S-IO-6 at -0.5 to -0.8 V . (d) Urea yields obtained over Vo-S-IO-6 using different feedstocks at -0.6 V versus RHE. (e) UV-vis absorbance spectra of electrolytes with different feedstocks. (f) Urea synthesis performance and CA curves of Vo-S-IO-6 during 5 consecutive recycles with KNO_3 and CO_2 feeding gas at -0.6 V versus RHE. (f) Comparison of FE between reported catalytic systems and Vo-S-IO-6 (see details in Table S1).

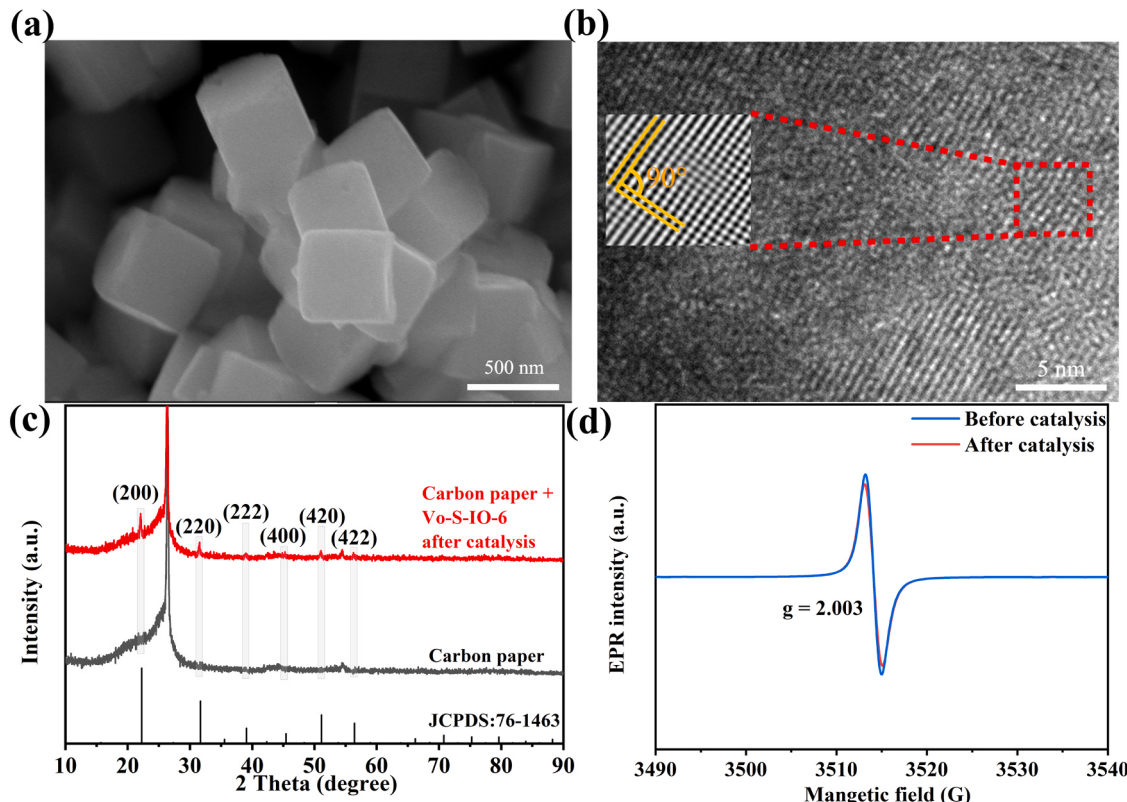


Fig. 5. (a) SEM image, (b) HRTEM image, (c) XRD patterns, and (d) EPR spectra of Vo-S-IO-6 after 5 reactions.

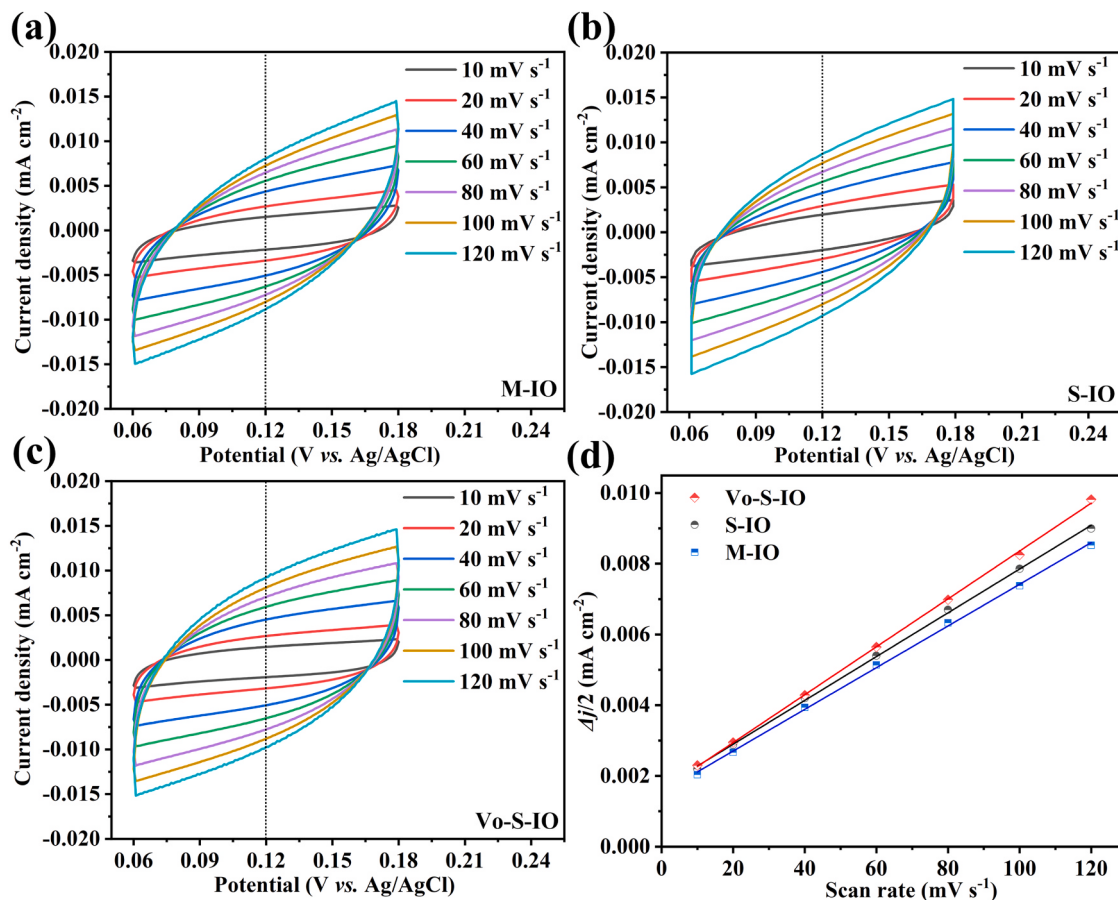
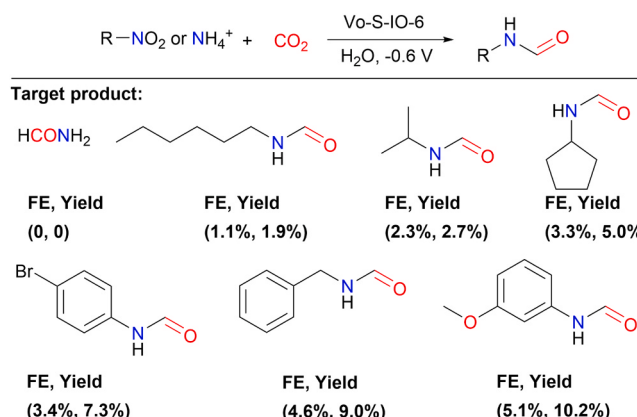


Fig. 6. Electrochemically active surface area (ECSA) tests. cyclic voltammograms for (a) M-IO, (b) S-IO, and (c) Vo-S-IO. (d) Charging current density differences $\Delta j/2$ plotted against scan rates.



Scheme 1. Electrocatalytic reductive C–N coupling of CO_2 and nitro compounds to synthesize *N*-formamides over Vo-S-IO-6. Reaction conditions: All reactions involving the reductive *N*-formylation of organic nitro-compounds with CO_2 were conducted at -0.6 V vs RHE in CO_2 -saturated 0.1 M KHCO_3 with 20 mM of the N source. All products were determined by GC-MS.

(**Scheme 1**). No *N*-formamide product was detected when NH_4^+ was used as the N source, indicating that the C–N coupling took place at a relatively lower oxidation state (i.e., $^*\text{NOR}$) rather than the over-reduced species (e.g., NH_3 or NH_4^+), which is consistent with the conversion process of urea synthesis. However, when nitro-compounds were chosen as the N sources, the corresponding *N*-formamide products were observed in moderate FE (1.1–5.1%, **Scheme 1**), as identified by gas chromatography-mass spectrometry (GC-MS) (**Figs. S21–26**). The

obtained results are comparable to those (FE: 0.6–9.8%) of the previously reported electrocatalytic systems using primary/secondary amines and CO_2 as the starting materials [47]. The electrocatalyst performance may be impeded by the relatively low solubility of the organic substrates in aqueous or water-containing electrolytes, which would be one of the key factors for further optimization of the overall conversion efficiency.

3.3. The synergy mechanism of facets and Vo

Based on experimental results, the synergistic role of crystal faces and Vo in the activation of key intermediates were speculated to be the reason for the pronounced electrocatalytic activity. To reveal the origin of the superior catalytic activity of Vo-SI-O-6, DFT calculations were performed. According to the XRD and EPR results, {110} facets, {100} facets, and {100} facets with Vo were used as models for M-IO, SI-O, and Vo-SI-O-6, respectively.

3.3.1. {100} facets-mediated C–N coupling

To understand the effect of different IO facets on the catalytic efficiency, differential charge densities of M-IO, S-IO and the key intermediate ($^*\text{NO}_2$) during the C–N coupling process were calculated. Results showed that the electrons of the two coordinately unsaturated In atoms on the {100} facets could be transferred to $^*\text{NO}_2$, leading to effective activation of $^*\text{NO}_2$, which may account for the intrinsic activity of the C–N coupling (**Fig. 7b**). Meanwhile, CO_2 was activated by forming a specific conformation (In-O-C-O-In) on the {100} facets, facilitating the electron transfer to $^*\text{CO}_2$ (**Fig. 7c**). C–N coupling can therefore undergo smoothly through the direct reaction between the intermediates $^*\text{NO}_2$ and $^*\text{CO}_2$. While on {110} facets, $^*\text{NO}_2$ exhibits weaker adsorption (**Fig. S27**, adsorption energy $E_{\text{ads}} = -0.936 \text{ eV}$ vs. $E_{\text{ads}} = -1.752 \text{ eV}$ on

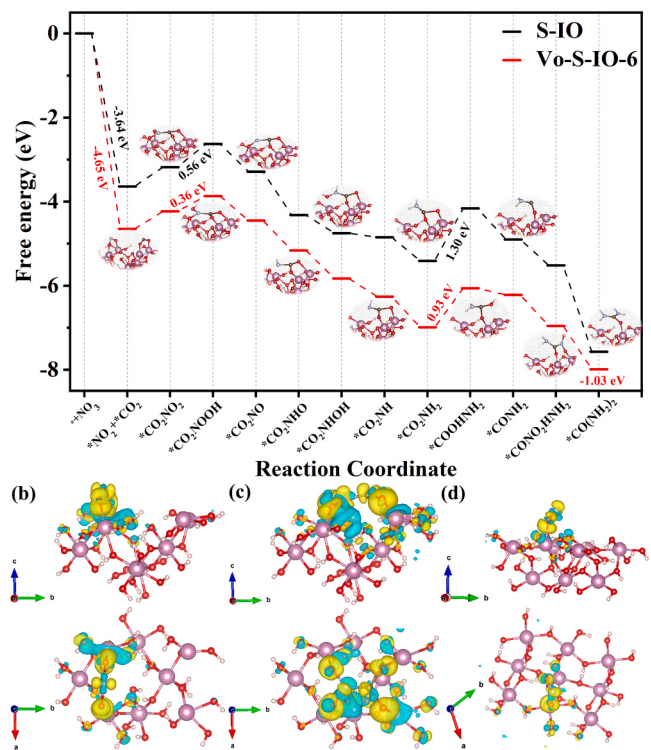


Fig. 7. Mechanism analysis of electrocatalytic urea synthesis from CO_2 and nitrate. (a) Free energy plots of S-IO and Vo-S-IO-6 for the electrosynthesis of urea at 0 V versus RHE. Side view and top view of the charge density difference of the (b) S-IO upon the adsorption of a $^*\text{NO}_2$ on the {100} facets, (c) upon the adsorption of a $^*\text{CO}_2\text{NO}_2$ on the {100} facets of S-IO, and (d) upon the adsorption of a $^*\text{NO}_2$ on the {110} facets of M-IO. The equivalent surfaces show the build-up (yellow) and exhaustion (cyan) of charge in real space respectively.

{100} facets) with only limited charge transfer to $^*\text{NO}_2$ (Fig. 7d). The free energy for protonation and coupling of $^*\text{NO}_2$ and $^*\text{CO}_2$ was calculated and summarized in Fig. 8. Coupling of $^*\text{NO}_2$ and $^*\text{CO}_2$ is favored on {100} facet with a lower free energy ($\Delta G = 0.32$ eV) compared to protonation ($\Delta G = 0.57$ eV ($^*\text{HNO}_2$), $\Delta G = 0.36$ eV ($^*\text{COOH}$)). However, on the {110} facet, the coupling free energy ($\Delta G = 1.47$ eV) of $^*\text{CO}_2$ and $^*\text{NO}_2$ is much higher than on the {100} facet (Fig. 8a). Meanwhile, the -OH groups in two adjacent In sites on the {110} facets (Fig. S28) are not beneficial for the C–N coupling during urea electro-synthesis, which can also be supported by the reduced urea yield and FE (Fig. S8). These results indicated that the {100} facets enhanced the adsorption of intermediates ($^*\text{NO}_2$ and $^*\text{CO}_2$) and inhibited their protonation, thus facilitating the coupling of $^*\text{NO}_2$ and $^*\text{CO}_2$.

The free energy diagrams of the reaction pathway were then calculated at the lowest energy on S-IO and Vo-SI-O-6 to reveal the effect of oxygen vacancy on {100} facets (Fig. 7a & S29). NO_3^- was first reduced to $^*\text{NO}_2$ intermediate on the {100} facets of Vo-S-IO-6 ($\Delta G = -4.65$ eV). On the contrary, the reduction of CO_2 to CO was an endothermic process ($\Delta G = 0.42$ eV, Fig. 8b), indicating that the reduction of NO_3^- to $^*\text{NO}_2$ is more favored on Vo-S-IO-6 catalyst compared to the reduction of CO_2 at the initial electrocatalytic stage. Compared with S-IO, Vo-S-IO showed a relatively higher Gibbs free energy for the formation of $^*\text{NO}_2$ ($\Delta G = -3.64$ eV), indicating that the presence of Vo benefits the reduction of NO_3^- to $^*\text{NO}_2$. The adsorbed $^*\text{NO}_2$ intermediate can further couple with CO_2^* to generate $^*\text{CO}_2\text{NO}_2$ or combine with H^* to form $^*\text{HNO}_2^*$ ($\Delta G = 0.32$ eV ($^*\text{CO}_2\text{NO}_2$) vs $\Delta G = 0.57$ eV ($^*\text{HNO}_2$), Fig. 8a). Therefore, the generation of $^*\text{CO}_2\text{NO}_2$ is thermodynamically favorable on {100} facets, remarkably benefiting urea production. The fact that urea cannot be obtained with NH_4^+ (200 ppm) as substrate in CO_2 -saturated 0.1 M K_2SO_4 with Vo-S-IO-6 catalyst also supports this route by excluding the possibility of obtaining urea from NH_4^+ (Fig. S30). Protonation of $^*\text{CO}_2\text{NO}_2$ can be significantly enhanced by introducing Vo with a much lower energy barrier. The protonation process first occurs in the $-\text{NO}_2$ part of $^*\text{CO}_2\text{NO}_2$ to form the intermediate $^*\text{CO}_2\text{NO}_2$. The energy barrier for this step is 0.36 eV and 0.56 eV for S-IO and Vo-SI-O-6, respectively. Further protonation of the $-\text{CO}_2$ part of $^*\text{CO}_2\text{NH}_2$ is endothermic with the highest free energy barrier (0.93 eV), which is a rate-determining step in the entire electro-synthesis of urea. The subsequent steps (the generation of the $^*\text{CONH}_2$ intermediate, C–N coupling, and the protonation of $^*\text{CONO}_2\text{NH}_2$ to generate $^*\text{CO}(\text{NH}_2)_2$) are thermodynamically favorable ($\Delta G = -1.03$ eV) (Fig. 7a). In brief, from a thermodynamic view, the introduction of Vo significantly can reduce the free energy barrier of $^*\text{CO}_2\text{NO}_2$ protonation to benefit the formation of urea.

3.3.2. Vo-accelerated protonation of $^*\text{CO}_2\text{NH}_2$ intermediate (rate-determining step)

As the protonation of $^*\text{CO}_2\text{NH}_2$ occurs on the coordinately unsaturated In atoms near Vo and involves the cleavage of the In–O bond. The electronegativity of In element in Vo-S-IO-6 and S-IO was further analyzed using Bader charge (Fig. 9a). The results showed that the introduction of Vo reduced the positivity of the adjacent In atoms, leading to a weakened bonding interaction between the Lewis base O in $^*\text{CO}_2\text{NH}_2$ intermediate and In atoms on the catalyst surface. In addition, the charge differential density, which reflects the electron redistribution of the In atoms around Vo (Fig. S31), further proved that Vo engineering could effectively tune the local electronic environment around the catalytic sites. To further clarify the Vo enhancement effect, the density of states (DOS) of In atoms bound to O atoms of the $^*\text{CO}_2\text{NH}_2$ intermediate were analyzed. The obtained DOS of the s and p orbitals of In atoms in Vo-S-IO-6 and S-IO are presented in Fig. 9b-e. Compared with S-IO, the electron density of In1 atom of Vo-S-IO-6 was reconfigured, leading to

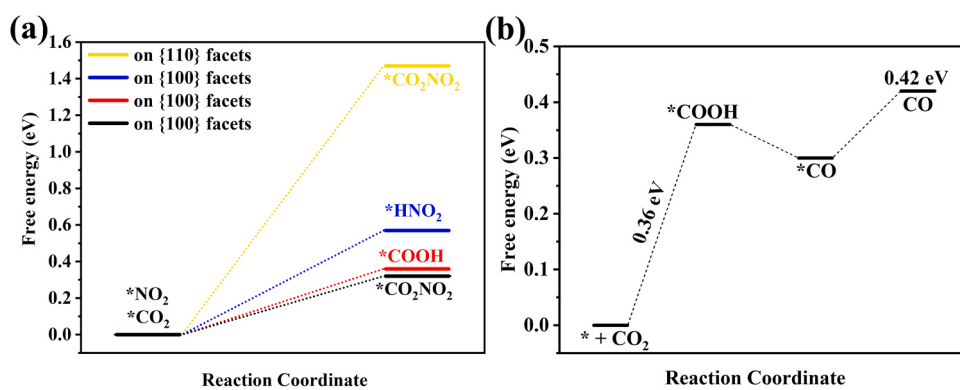


Fig. 8. Free energy profiles of (a) coupling on the {100} and {110} facets and protonation on the {100} of $^*\text{CO}_2$ and $^*\text{NO}_2$, and (b) CO_2 reduction to CO over Vo-S-IO.

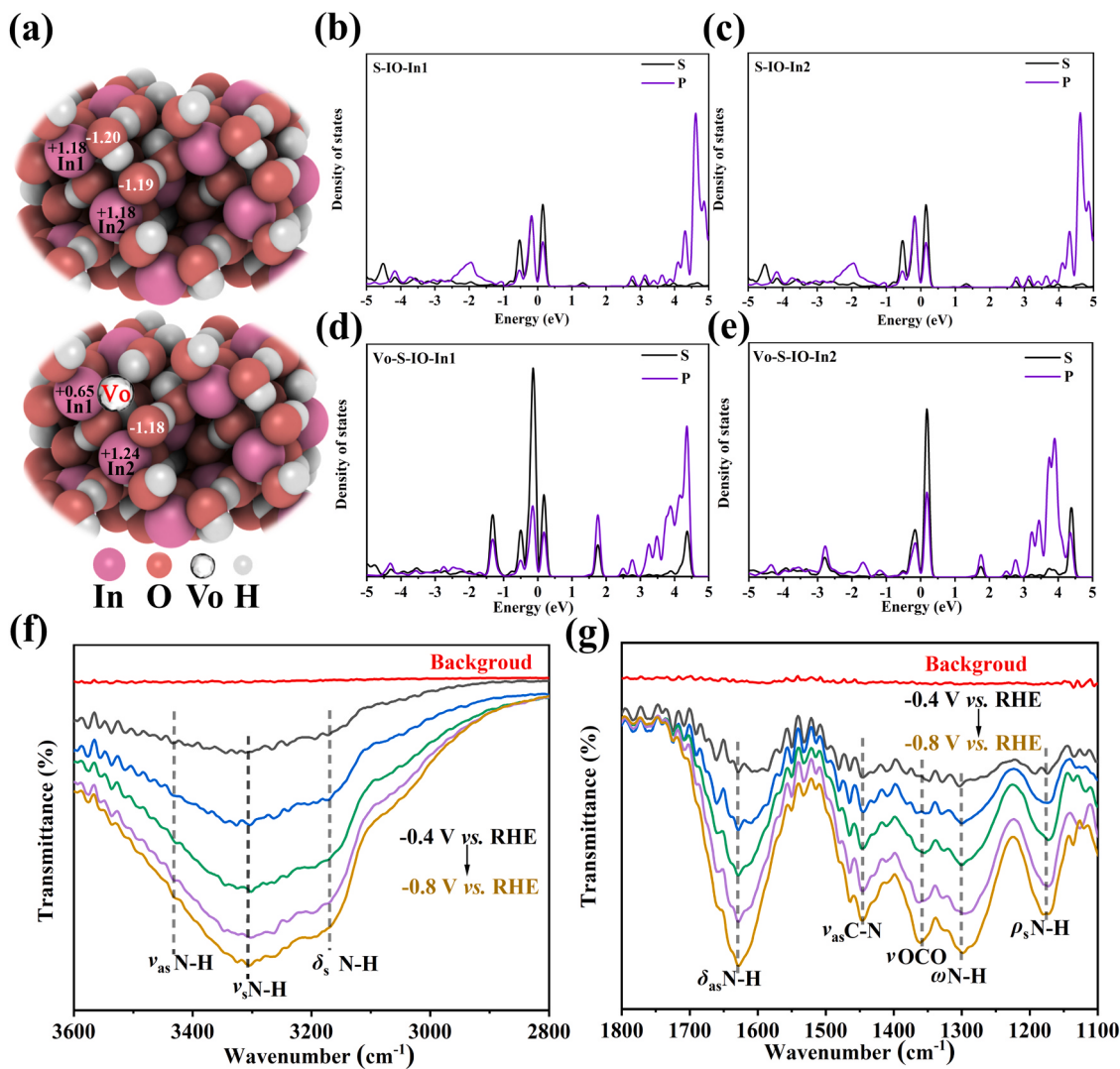


Fig. 9. (a) Bader charge analysis of S-IO and Vo-S-IO-6. DOS of the In atoms of S-IO (b and c) and Vo-S-IO-6 (d and e) in contact with O in $^{*}\text{CO}_2\text{NH}_2$. *In situ* ATR-FTIR spectra at an applied voltage (-0.4 to -0.8 V) for the synthesis of urea from NO_3^- -integrated electrocatalytic CO_2 reduction over Vo-S-IO-6: Infrared signals in the range of 2800 – 3600 cm^{-1} (f), and 1100 – 1800 cm^{-1} (g).

an increase in bonding states and a decrease in antibonding states (Fig. 9d). Therefore, the interaction of $^{*}\text{CO}_2\text{NH}_2$ with In1 atoms is weakened by Vo [48]. In addition, the DOS of In2 atom of S-IO was almost the same as that of In1 atom (Fig. 9b-c). For the In2 atom of Vo-S-IO, contrary to the In1 atom, the bonding state decreased and the antibonding state increased (Fig. 9e). These results indicated that the O atom bound to the In1 atom in $^{*}\text{CO}_2\text{NH}_2$ was more likely to undergo cleavage on Vo-S-IO-6, thereby promoting the protonation of $^{*}\text{CO}_2\text{NH}_2$ [25]. The above theoretical calculations demonstrated that Vo engineering could significantly tune the electronic structure around the catalytic sites to accelerate the cleavage of In–O bond in Vo-S-IO-6 adsorbed $^{*}\text{CO}_2\text{NH}_2$, thereby benefiting the protonation process and boosting the electrocatalytic performance of urea synthesis.

In situ ATR-FTIR technique was adopted to monitor the urea electrosynthesis process catalyzed by Vo-S-IO-6 to gain more detailed information on the reaction process. Infrared signals were collected from 800 cm^{-1} to 4000 cm^{-1} during a negative scan from -0.4 to -0.8 V (Fig. S32, Fig. 9f-g). The characteristic absorption bands of the asymmetric stretching vibration (ν_{as}), symmetrical stretching vibration (ν_s), symmetrical bending vibration (δ_s), and asymmetric bending vibration (δ_{as}) of the N–H bond could be found at 3440 , 3368 , 3187 , and 1635 cm^{-1} respectively [49,50]. In addition, the infrared absorption

bands at 1307 and 1170 cm^{-1} observed at -0.5 V vs. RHE were assigned to the out-of-plane wagging vibration (ω) and rocking vibrations (ρ) of N–H bond, respectively [51], demonstrating the formation of NH_2 . Besides, the ν_{as} absorption sideband of the C–N bond was observed at 1419 cm^{-1} [52], and the absorption intensity increased with increasing negative potential. In addition, the -OCO- vibrational band appeared at 1396 cm^{-1} at -0.4 V [24,25], suggesting the formation of the $^{*}\text{CO}_2\text{NH}_2$ intermediate. Overall, the *in-situ* ATR-FTIR results illustrated that urea was produced via the C–N coupling route, consistent with the results from electrocatalytic experiments and DFT calculations.

4. Conclusions

In summary, a robust Vo-S-IO-6 electrocatalyst simultaneously bearing $\{100\}$ facets and Vo was fabricated to show an unprecedented FE of 60.6% with a high production rate of 910.4 $\mu\text{g h}^{-1} \text{mg}_{\text{cat}}^{-1}$ in urea electrosynthesis from nitrate and CO_2 . DFT calculations indicated that the superior efficiency of the electrocatalyst could be due to the synergistic effect of facets and the Vo. The facet-mediated C–N coupling guaranteed the outstanding selectivity of urea. On $\{100\}$ facets, $^{*}\text{NO}_2$ and $^{*}\text{CO}_2$ intermediates could be efficiently stabilized and activated by a local In–O–x–O–In ($x = \text{C}$ or N) configuration, thus finishing direct C–N

coupling instead of protonation of the above two intermediates. In addition, the introduction of Vo caused a reconfiguration of the electron density of In atom in Vo-S-IO-6. The weakened In–O bond lowered the energy barrier of protonation of $^{18}\text{O}\text{CO}_2\text{NH}_2$ (rate-determining step), leading to a relatively higher activity. This study reveals the synergistic effect of crystal faces and Vo on promoting the performance of electrocatalytic urea synthesis, which provides new ideas for local environmental engineering to construct efficient electrocatalysts.

CRediT authorship contribution statement

Zhengyi Li: Conceptualization, Methodology, Formal analysis, Investigation, Writing – review & editing. **Peng Zhou:** Writing – review & editing. **Min Zhou:** Investigation. **Hao Jiang:** Software. **Hu Li:** Supervision, Conceptualization, Methodology, Writing – review & editing. **Shengqi Liu:** Discussion. **Heng Zhang:** Formal analysis. **Yang Song:** Supervision, Writing – review & editing. **Zehui Zhang:** Writing – review & editing.

Declaration of Competing Interest

The authors declare that they have no known competing financial interests or personal relationships that could have appeared to influence the work reported in this paper.

Data availability

Data will be made available on request.

Acknowledgements

The study was funded by the Guizhou Provincial S&T Project (ZK [2022]011), National Natural Science Foundation of China (21908033), and Fok Ying-Tong Education Foundation (161030).

Appendix A. Supporting information

Supplementary data associated with this article can be found in the online version at [doi:10.1016/j.apcatb.2023.122962](https://doi.org/10.1016/j.apcatb.2023.122962).

References

- Nitopi, E. Bertheussen, S.B. Scott, X. Liu, A.K. Engstfeld, S. Horch, B. Seger, I.E. L. Stephens, K. Chan, C. Hahn, J.K. Norskov, T.F. Jaramillo, I. Chorkendorff, Progress and perspectives of electrochemical CO_2 reduction on copper in aqueous electrolyte, *Chem. Rev.* 119 (2019) 7610–7672, <https://doi.org/10.1021/acs.chemrev.8b00705>.
- Wei, R. Yao, Y. Han, Q. Ge, J. Sun, Towards the development of the emerging process of CO_2 heterogenous hydrogenation into high-value unsaturated heavy hydrocarbons, *Chem. Soc. Rev.* 50 (2021) 10764–10805, <https://doi.org/10.1039/D1EE0260K>.
- Climate change 2014: mitigation of climate change. Contribution of working group III to the fifth assessment report of the Intergovernmental Panel on Climate Change (2014) New York.
- Akhade, N. Singh, O.Y. Gutierrez, J. Lopez-Ruiz, H. Wang, J.D. Holladay, Y. Liu, A. Karkamkar, R.S. Weber, A.B. Padmaperuma, M.S. Lee, G.A. Whyatt, M. Elliott, J.E. Holladay, J.L. Male, J.A. Lercher, R. Rousseau, V.A. Glezakou, Electrocatalytic hydrogenation of biomass-derived organics: a review, *Chem. Rev.* 120 (2020) 11370–11419, <https://doi.org/10.1021/acs.chemrev.0c00158>.
- W.S. Lucas, R.G. Grim, S.A. Tacey, C.A. Downes, J. Hasse, A.M. Roman, C. A. Farberow, J.A. Schaidle, A. Holewinski, Electrochemical routes for the valorization of biomass-derived feedstocks: from chemistry to application, *ACS Energy Lett.* 6 (2021) 1205–1270, <https://doi.org/10.1021/acsenergylett.0c02692>.
- X. Zhang, E.A. Davidson, D.L. Mauzerall, T.D. Searchinger, P. Dumas, Y. Shen, Managing nitrogen for sustainable development, *Nature* 528 (2015) 51–59, <https://doi.org/10.1038/nature15743>.
- M. Chen, Z.J. Wu, J. Song, H.C. Xu, Electrocatalytic allylic C–H alkylation enabled by a dual-function cobalt catalyst, *Angew. Chem. Int. Ed.* 61 (2022), e202115954, <https://doi.org/10.1002/anie.202115954>.
- X. Lu, K.H. Wu, B. Zhang, J. Chen, F. Li, B.J. Su, P. Yan, J.M. Chen, W. Qi, Highly efficient electro-reforming of 5-hydroxymethylfurfural on vertically oriented nickel nanosheet/carbon hybrid catalysts: structure-function relationships, *Angew. Chem. Int. Ed.* 60 (2021) 14528–14535, <https://doi.org/10.1002/anie.202102359>.
- Wang, T. Li, C. Yang, M. Chen, A. Guan, L. Yang, S. Li, X. Lv, Y. Wang, G. Zheng, Electrocatalytic methane oxidation greatly promoted by chlorine intermediates, *Angew. Chem. Int. Ed.* 60 (2021) 17398–17403, <https://doi.org/10.1002/anie.202105523>.
- Z.J. Schiffer, K. Manthiram, Electrification and decarbonization of the chemical industry, *Joule* 1 (2017) 10–14, <https://doi.org/10.1016/j.joule.2017.07.008>.
- C. Tang, Y. Zheng, M. Jaroniec, S.Z. Qiao, Electrocatalytic refinery for sustainable production of fuels and chemicals, *Angew. Chem. Int. Ed.* 60 (2021) 19572–19590, <https://doi.org/10.1002/anie.202101522>.
- J. Li, Y. Zhang, K. Kuruvinashetti, N. Kornienko, Construction of C–N bonds from small-molecule precursors through heterogeneous electrocatalysis, *Nat. Rev. Chem.* 6 (2022) 303–319, <https://doi.org/10.1038/s41570-022-00379-5>.
- B.M. Comer, P. Fuentes, C.O. Dinkpa, Y.-H. Liu, C.A. Fernandez, P. Arora, M. Realf, U. Singh, M.C. Hatzell, A.J. Medford, Prospects and challenges for solar fertilizers, *Joule* 3 (2019) 1578–1605, <https://doi.org/10.1016/j.joule.2019.05.001>.
- X. Zhu, X. Zhou, Y. Jing, Y. Li, Electrochemical synthesis of urea on MBenes, *Nat. Commun.* 12 (2021) 4080, <https://doi.org/10.1038/s41467-021-24400-5>.
- H. Zhang, Z. Sun, Y.H. Hu, Steam reforming of methane: current states of catalyst design and process upgrading, *Renew. Sustain. Energy Rev.* 149 (2021), 111330, <https://doi.org/10.1016/j.rser.2021.111330>.
- C. Smith, A.K. Hill, L. Torrente-Murciano, Current and future role of Haber–Bosch ammonia in a carbon-free energy landscape, *Energy Environ. Sci.* 13 (2020) 331–344, <https://doi.org/10.1039/c9ee02873k>.
- S. Gidley, S.P.S. Badwal, A. Kulkarni, Review of electrochemical ammonia production technologies and materials, *Int. J. Hydrog. Energy* 38 (2013) 14576–14594, <https://doi.org/10.1016/j.ijhydene.2013.09.054>.
- C. Chen, X. Zhu, X. Wen, Y. Zhou, L. Zhou, H. Li, L. Tao, Q. Li, S. Du, T. Liu, D. Yan, C. Xie, Y. Zou, Y. Wang, R. Chen, J. Huo, Y. Li, J. Cheng, H. Su, X. Zhao, W. Cheng, Q. Liu, H. Lin, J. Luo, J. Chen, M. Dong, K. Cheng, C. Li, S. Wang, Coupling N_2 and CO_2 in H_2O to synthesize urea under ambient conditions, *Nat. Chem.* 12 (2020) 717–724, <https://doi.org/10.1038/s41557-020-0481-9>.
- M. Yuan, J. Chen, Y. Bai, Z. Liu, J. Zhang, T. Zhao, Q. Shi, S. Li, X. Wang, G. Zhang, Electrochemical C–N coupling with perovskite hybrids toward efficient urea synthesis, *Chem. Sci.* 12 (2021) 6048–6058, <https://doi.org/10.1039/DSC01467F>.
- M. Yuan, J. Chen, Y. Bai, Z. Liu, J. Zhang, T. Zhao, Q. Wang, S. Li, H. He, G. Zhang, Unveiling electrochemical urea synthesis by co-activation of CO_2 and N_2 with Mott–Schottky heterostructure catalysts, *Angew. Chem. Int. Ed.* 60 (2021) 10910–10918, <https://doi.org/10.1002/anie.202101275>.
- M. Yuan, J. Chen, Y. Xu, R. Liu, T. Zhao, J. Zhang, Z. Ren, Z. Liu, C. Streb, H. He, Highly selective electroreduction of N_2 and CO_2 to urea over artificial frustrated Lewis pairs, *Energy Environ. Sci.* 14 (2021) 6605–6615, <https://doi.org/10.1039/DIE02485J>.
- M. Yuan, H. Zhang, Y. Xu, R. Liu, R. Wang, T. Zhao, J. Zhang, Z. Liu, H. He, C. Yang, S. Zhang, G. Zhang, Artificial frustrated Lewis pairs facilitating the electrochemical N_2 and CO_2 conversion to urea, *Chem. Catal.* 2 (2022) 309–320, <https://doi.org/10.1016/j.jchecat.2021.11.009>.
- M. Yuan, J. Chen, H. Zhang, Q. Li, L. Zhou, C. Yang, R. Liu, Z. Liu, S. Zhang, G. Zhang, Host–guest molecular interaction promoted urea electrosynthesis over a precisely designed conductive metal–organic framework, *Energy Environ. Sci.* 15 (2022) 2084–2095, <https://doi.org/10.1039/DIE03918K>.
- C. Lv, L. Zhong, H. Liu, Z. Fang, C. Yan, M. Chen, Y. Kong, C. Lee, D. Liu, S. Li, J. Liu, L. Song, G. Chen, Q. Yan, G. Yu, Selective electrocatalytic synthesis of urea with nitrate and carbon dioxide, *Nat. Sustain.* 4 (2021) 868–876, <https://doi.org/10.1038/s41893-021-00741-3>.
- C. Lv, C. Lee, L. Zhong, H. Liu, J. Liu, L. Yang, C. Yan, W. Yu, H.H. Hng, Z. Qi, L. Song, S. Li, K.P. Loh, Q. Yan, G. Yu, A defect engineered electrocatalyst that promotes high-efficiency urea synthesis under ambient conditions, *ACS Nano* 16 (2022) 8213–8222, <https://doi.org/10.1021/acsnano.2c01956>.
- Meng, X. Ma, C. Wang, Y. Wang, R. Yang, J. Shao, Y. Huang, Y. Yu, B. Zhang, Y. Yu, Oxide-derived core-shell $\text{Cu}@\text{Zn}$ nanowires for urea electrosynthesis from carbon dioxide and nitrate in water, *ACS Nano* 16 (2022) 9095–9104, <https://doi.org/10.1021/acsnano.2c01177>.
- Chen, S. Zhang, X. Bu, R. Zhang, Q. Quan, Z. Lai, W. Wang, Y. Meng, D. Yin, S. Yip, C. Liu, C. Zhi, J.C. Ho, Synergistic modulation of local environment for electrochemical nitrate reduction via asymmetric vacancies and adjacent ion clusters, *Nano Energy* 98 (2022), 107338, <https://doi.org/10.1016/j.nano.2022.107338>.
- Wang, G. Liu, L. Wang, Crystal facet engineering of photoelectrodes for photoelectrochemical water splitting, *Chem. Rev.* 119 (2019) 5192–5247, <https://doi.org/10.1021/acs.chemrev.8b00584>.
- Gao, Q. Wu, X. Liang, Z. Wang, Z. Zheng, P. Wang, Y. Liu, Y. Dai, M. H. Whangbo, B. Huang, Cu_2O nanoparticles with both {100} and {111} facets for enhancing the selectivity and activity of CO_2 electroreduction to ethylene, *Adv. Sci.* 7 (2020) 1902820, <https://doi.org/10.1002/adv.201902820>.
- Lim, C.Y. Liu, J. Park, Y.H. Liu, T.P. Senftle, S.W. Lee, M.C. Hatzell, Structure sensitivity of Pd facets for enhanced electrochemical nitrate reduction to ammonia, *ACS Catal.* 11 (2021) 7568–7577, <https://doi.org/10.1021/ascata.1c01413>.
- Ke, J. Zhao, M. Chi, M. Wang, X. Kong, Q. Chang, W. Zhou, C. Long, J. Zeng, Z. Geng, Facet-dependent electrooxidation of propylene into propylene oxide over Ag_3PO_4 crystals, *Nat. Commun.* 13 (2022) 932, <https://doi.org/10.1038/s41467-022-28516-0>.

[32] N. Cao, Y. Quan, A. Guan, C. Yang, Y. Ji, L. Zhang, G. Zheng, Oxygen vacancies enhanced cooperative electrocatalytic reduction of carbon dioxide and nitrite ions to urea, *J. Colloid Interface Sci.* 577 (2020) 109–114, <https://doi.org/10.1016/j.jcis.2020.05.014>.

[33] C. Mao, J. Wang, Y. Zou, G. Qi, J.Y. Yang Loh, T. Zhang, M. Xia, J. Xu, F. Deng, M. Ghoussoub, N.P. Kherani, L. Wang, H. Shang, M. Li, J. Li, X. Liu, Z. Ai, G. A. Ozin, J. Zhao, L. Zhang, Hydrogen spillover to oxygen vacancy of $\text{TiO}_{2-x}\text{H}_y/\text{Fe}$: breaking the scaling relationship of ammonia synthesis, *J. Am. Chem. Soc.* 142 (2020) 17403–17412, <https://doi.org/10.1021/jacs.0c06118>.

[34] H. Yu, F. Chen, X. Li, H. Huang, Q. Zhang, S. Su, K. Wang, E. Mao, B. Mei, G. Mul, T. Ma, Y. Zhang, Synergy of ferroelectric polarization and oxygen vacancy to promote CO_2 photoreduction, *Nat. Commun.* 12 (2021) 4594, <https://doi.org/10.1038/s41467-021-24882-3>.

[35] Y. Chen, S. Chen, Z. Zhou, N. Tian, Y. Jiang, S. Sun, Y. Ding, Z. Wang, Tuning the shape and catalytic activity of Fe nanocrystals from rhombic dodecahedra and tetragonal bipyramids to cubes by electrochemistry, *J. Am. Chem. Soc.* 131 (2009) 10860–10862, <https://doi.org/10.1021/ja904225q>.

[36] J. Liu, G. Chen, Y. Yu, Y. Wu, M. Zhou, W. Zhang, H. Qin, C. Lv, W. Fu, Controllable and facile synthesis of nearly monodisperse 18-facet indium hydroxide polyhedra, *New J. Chem.* 39 (2015) 1930–1937, <https://doi.org/10.1039/c4nj01996b>.

[37] Q. Miao, C. Nitsche, H. Orton, M. Overhand, G. Otting, M. Ubbink, Paramagnetic chemical probes for studying biological macromolecules, *Chem. Rev.* 122 (2022) 9571–9642, <https://doi.org/10.1021/acs.chemrev.1c00708>.

[38] R. Schmitt, A. Nenning, O. Kraynis, R. Korobko, A.I. Frenkel, I. Lubomirsky, S. M. Haile, J.L.M. Rupp, A review of defect structure and chemistry in ceria and its solid solutions, *Chem. Soc. Rev.* 49 (2020) 554–592, <https://doi.org/10.1039/c9cs00588a>.

[39] B. Hu, M. Hu, Q. Guo, K. Wang, X. Wang, In-vacancy engineered plate-like In(OH)_3 for effective photocatalytic reduction of CO_2 with H_2O vapor, *Appl. Catal. B Environ.* 253 (2019) 77–87, <https://doi.org/10.1016/j.apcatb.2019.04.046>.

[40] H. Zhao, W. Yin, M. Zhao, Y. Song, H. Yang, Hydrothermal fabrication and enhanced photocatalytic activity of hexagram shaped InOOH nanostructures with exposed {020} facets, *Appl. Catal. B* 130 (2013) 178–186, <https://doi.org/10.1016/j.apcatb.2012.10.027>.

[41] A. Gurlo, D. Dzivenko, M. Andrade, R. Riedel, S. Lauterbach, H.-J. Kleebe, Pressure-induced decomposition of indium hydroxide, *J. Am. Chem. Soc.* 132 (2010) 12674–12678, <https://doi.org/10.1021/ja104278p>.

[42] T. Yan, N. Li, L. Wang, W. Ran, P.N. Duchesne, L. Wan, N.T. Nguyen, L. Wang, M. Xia, G.A. Ozin, Bismuth atom tailoring of indium oxide surface frustrated Lewis pairs boosts heterogeneous CO_2 photocatalytic hydrogenation, *Nat. Commun.* 11 (2020) 6095, <https://doi.org/10.1038/s41467-020-19997-y>.

[43] V. Golovanov, M.A. Mäki-Jaskari, T.T. Rantala, G. Korotcenkov, V. Brinzari, A. Cornet, J. Morante, Experimental and theoretical studies of indium oxide gas sensors fabricated by spray pyrolysis, *Sens. Actuators B* 106 (2005) 563–571, <https://doi.org/10.1016/j.snb.2004.07.026>.

[44] L. He, T.E. Wood, B. Wu, Y. Dong, L.B. Hoch, L.M. Reyes, D. Wang, C. Kubel, C. Qian, J. Jia, K. Liao, P.G. O'Brien, A. Sandhel, J.Y. Loh, P. Szymanski, N. P. Kherani, T.C. Sum, C.A. Mims, G.A. Ozin, Spatial separation of charge carriers in $\text{In}_2\text{O}_{3-x}(\text{OH})_y$ nanocrystal superstructures for enhanced gas-phase photocatalytic activity, *ACS Nano* 10 (2016) 5578–5586, <https://doi.org/10.1021/acsnano.6b02346>.

[45] O. Martin, A.J. Martín, C. Mondelli, S. Mitchell, T.F. Segawa, R. Hauer, C. Drouilly, D. Curulla-Ferré, J. Pérez-Ramírez, Indium oxide as a superior catalyst for methanol synthesis by CO_2 hydrogenation, *Angew. Chem. Int. Ed.* 55 (2016) 6261–6265, <https://doi.org/10.1002/ange.201600943>.

[46] N. Rui, Z. Wang, K. Sun, J. Ye, Q. Ge, C.-j. Liu, CO_2 hydrogenation to methanol over $\text{Pd}/\text{In}_2\text{O}_3$: effects of Pd and oxygen vacancy, *Appl. Catal. B* 218 (2017) 488–497, <https://doi.org/10.1016/j.apcatb.2017.06.069>.

[47] C.L. Rooney, Y. Wu, Z. Tao, H. Wang, Electrochemical reductive N-methylation with CO_2 enabled by a molecular catalyst, *J. Am. Chem. Soc.* 143 (2021) 19983–19991, <https://doi.org/10.1021/jacs.1c10863>.

[48] J. Zhang, R. Yin, Q. Shao, T. Zhu, X. Huang, Oxygen vacancies in amorphous InO_x nanoribbons enhance CO_2 adsorption and activation for CO_2 electroreduction, *Angew. Chem. Int. Ed.* 58 (2019) 5609–5613, <https://doi.org/10.1002/anie.201900167>.

[49] R. Keuleers, H. Desseyn, B. Rousseau, C. Van Alsenoy, Vibrational analysis of urea, *J. Mater. Chem. A* 103 (1999) 4621–4630, <https://doi.org/10.1021/jp984180z>.

[50] D. Yue, Y. Jia, Y. Yao, J. Sun, Y. Jing, Structure and electrochemical behavior of ionic liquid analogue based on choline chloride and urea, *Electrochim. Acta* 65 (2012) 30–36, <https://doi.org/10.1016/j.electacta.2012.01.003>.

[51] Y. Yao, S. Zhu, H. Wang, H. Li, M. Shao, A spectroscopic study on the nitrogen electrochemical reduction reaction on gold and platinum surfaces, *J. Am. Chem. Soc.* 140 (2018) 1496–1501, <https://doi.org/10.1021/jacs.7b12101>.

[52] M. Manivannan, S. Rajendran, Investigation of inhibitive action of urea- Zn^{2+} system in the corrosion control of carbon steel in sea water, *Int. J. Eng. Sci. Technol.* 3 (2011) 8048–8060.